PCCP

Accepted Manuscript

This article can be cited before page numbers have been issued, to do this please use: S. R. Tachibana, L. Tang, Y. Wang, L. Zhu, W. Liu and C. Fang, *Phys. Chem. Chem. Phys.*, 2017, DOI: 10.1039/C6CP08821J.

ROYAL SOCIETY OF CHEMISTRY

rsc.li/pccp

View Article Online
DOI: 10.1039/C6CP08821J

Journal Name

ARTICLE

Tuning calcium biosensors with a single-site mutation: Structural dynamics insights from femtosecond Raman spectroscopy†

Sean R. Tachibana,‡[a] Longteng Tang,‡[a] Yanli Wang,[a] Liangdong Zhu,[ab] Weimin Liu,[ac] and Chong Fang*[ab]

Fluorescent protein biosensors are popular reporters for biological processes and life sciences, but their fundamental working mechanisms remain unclear. To characterize the functional fluorescence events on their native timescales, we implemented the wavelength-tunable femtosecond stimulated Raman spectroscopy (FSRS) to shed light on a blue-green emission-ratiometric fluorescent protein based Ca^{2+} biosensor with a single Pro377Arg mutation. The transient Raman modes of the embedded chromophore from ca. 1000—1650 cm^{-1} exhibit characteristic intensity and frequency dynamics which infer the underlying atomic motions and photochemical reaction stages. Our experimental study reveals the hidden structural inhomogeneity of the protein local environment upon Ca^{2+} binding with the mutated arginine residue trapping multiple chromophore subpopulations, which manifest distinct time constants of ~16 and 90 ps for excited state proton transfer (ESPT) following 400 nm photoexcitation. The altered ESPT reaction pathways and emission properties of the Ca^{2+} biosensor represent the foundational step of rationally designing advanced fluorescent protein biosensors to tune their functionalities by site-specifically altering the local environment (e.g., active site) of the embedded chromophore.

Received 00th January 20xx,
Accepted 00th January 20xx

DOI: 10.1039/x0xx00000x

www.rsc.org/

Introduction

Modern biological imaging and life sciences have benefited tremendously from the development of fluorescent proteins (FPs) and the FP-based biosensors.[1-5] Among them, genetically encoded calcium indicators for optical imaging (GECOs) belong to a family of circularly permuted (cp)FP-based biosensors.[6,7] The GECOs consist of three major subunits, calmodulin (CaM), a binding client such as M13 peptide from myosin light chain kinase, and cpGFP. As CaM binds calcium ions (Ca^{2+}), it wraps itself around M13 and blocks the adjacent β-barrel opening which affects the emission properties of the biosensor. These highly functional protein biosensors have enabled advanced bioimaging with different scanning and modelling procedures, but their intrinsic fluorescence mechanisms remain one of the crucial and governing aspects for future rational design. The challenges to achieve such level of fundamental understanding lie at the experimental difficulty of tracking atomic motions in the electronic excited state.[8] When such information becomes available with the invent of suitable techniques, it is desirable to examine the molecular structural dynamics basis with site specificity so detailed reaction coordinates can be dissected without overlapping contributions from a crowded protein environment.[9-13] This unique line of inquiry is thus biophysical chemistry in nature with a fundamental focus, making it an indispensable integral part of chemical sciences. Furthermore, instead of being a specialized effort to benchmark a model system, the practical implications of our results in revealing fluorescence modulation mechanisms and how they govern the biosensor imaging properties are directly applicable and beneficial for the broad science and engineering community.

To provide such mechanistic insights, we have developed femtosecond stimulated Raman spectroscopy (FSRS)[10,14-16] to study a dual-emission ratiometric Ca^{2+} biosensor, GEM-GECO1, with an autocatalytically formed Ser-Tyr-Gly (SYG) chromophore.[6,7] The FSRS technique enables us to go beyond the UV-Visible and fluorescence spectroscopy showing that the Ca^{2+}-free biosensor emits green but changes to blue upon Ca^{2+} binding. Our key finding was that excited state proton transfer (ESPT) in an "open" β-barrel on a ~30 picosecond (ps) timescale generates a deprotonated chromophore that emits green photons. With Ca^{2+} binding, conformationally changed CaM pushes its Pro377 to the interface, creating a hydrophobic environment near the GFP chromophore and inhibiting proton transfer.[17,18] The dominant structural motion that guides GEM-GECO1 out of the Franck-Condon (FC) region is a phenolic ring rocking.[17] This vibrational motion facilitates ESPT in the Ca^{2+}-free GEM-GECO1 biosensor as evinced by spectral oscillations. Because ESPT is a ubiquitous process in FPs which determines their overall function of fluorescence, this work holds a broad impact for the FP researchers, engineers as well as users.

[a] Oregon State University, Department of Chemistry, 263 Linus Pauling Science Centre (lab), 153 Gilbert Hall (office), Corvallis, OR 97331, USA. *E-mail: Chong.Fang@oregonstate.edu; Fax: +1 541 737 2062; Tel: +1 541 737 6704; Web: http://oregonstate.edu/colleges/chem/fang/
[b] Department of Physics, 301 Weniger Hall, Corvallis, OR 97331, USA.
[c] Current Address: School of Physical Science and Technology, ShanghaiTech University, Pudong, Shanghai 201210, P. R. China.

† Electronic Supplementary Information (ESI) available: Further discussion on the significance and perspective of this work, Figs. S1-S4 and Tables S1-S2, and additional references. See DOI: 10.1039/x0xx00000x

‡ These authors contributed equally to this work.

View Article Online
DOI: 10.1039/C6CP08821J
ARTICLE Journal Name

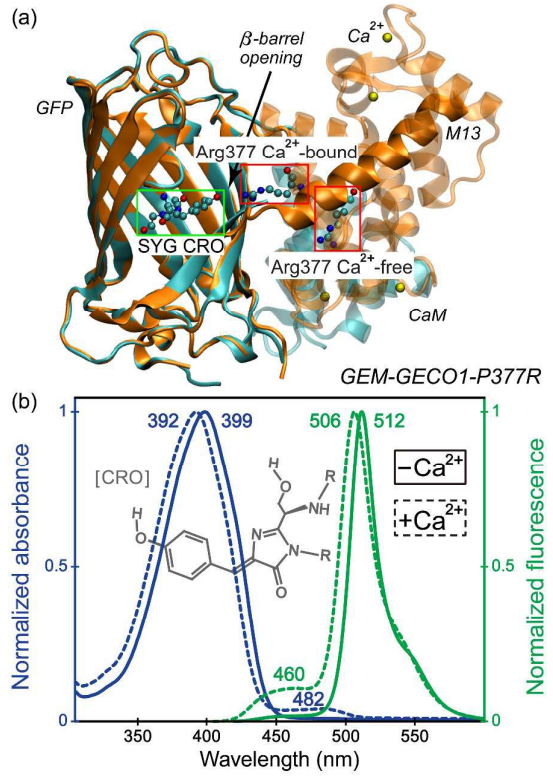

Fig. 1 Structure and optical properties of the GEM-GECO1-P377R biosensor. (a) The Ca^{2+}-free (cyan, PDB ID 3EKJ) and bound (orange, ID 3EVR) parent GCaMP2 structures modelling GFP chromophore [CRO] and CaM interfacial arginine residue highlighted by the coloured boxes. Four Ca^{2+} binding sites are shown. (b) Normalized absorption (blue) and emission (green) spectra of the biosensor in the Ca^{2+}-free (solid) and bound (dashed) state. The peak wavelengths are noted. The chemical structure of the SYG chromophore (grey) is depicted in the insert.

To delineate the role played by Pro377, Campbell and co-workers performed single-site mutagenesis at residue position 377 in GEM-GECO1, replacing proline with arginine (P377R).[17] Our experimental approach is to collect the conventional FSRS with an 800 nm Raman pump[10,17,19] to track the protonated chromophore A* modes after photoexcitation of the P377R (short for GEM-GECO1-P377R) biosensor, and then tune the Raman pump to visible range[16,20,21] to track the deprotonated chromophore I* modes as the ESPT reaction progresses. The comparison between the Ca^{2+}-free and bound biosensors infers calcium sensing mechanisms, while the contrast to GEM-GECO1 biosensor elucidates the functional role of residue 377. Notably, our recent results on an intensiometric biosensor G-GECO1.1 concern a different TYG chromophore which has an extra methyl group at the imidazolinone end.[20] That is why we focus our comparative analysis between GEM-GECO1 and its P377R mutant (i.e., change of one residue) so we can reliably discern the main effect of a single-site mutation in the vicinity of the conserved SYG chromophore. The conformational states and dynamics insights clearly involve the SYG chromophore and ESPT time constants which underlie intrinsic fluorescence modulation mechanism of the overall P377R biosensor.

Results and discussion

A. Steady-state and time-resolved spectroscopic characterization of the protein chimera biosensor in solution

Based on the parent GCaMP crystal structures in the Ca^{2+}-free state,[22,23] Arg377 is located in the CaM domain, far from the β-barrel opening and the embedded GFP chromophore (Fig. 1a). The Ca^{2+}-free P377R biosensor resembles GEM-GECO1 with the absorption maximum at 399 nm and the fluorescence maximum at 512 nm (Fig. 1b). Upon Ca^{2+} binding, the peaks blueshift to 392 and 506 nm, respectively, and the absorption shoulder at ~482 nm shows a slightly increased deprotonated chromophore (B) population in ground state (S_0). This blueshift of electronic features is commonly observed in GECOs,[7,17,20] indicating a stabilized chromophore in the Ca^{2+}-bound state with more electrostatic interactions including H-bonding. This creates a larger gap between S_0 to the first singlet excited state (S_1). Meanwhile, the 460 nm emission shoulder represents a subpopulation of protonated chromophore (A) that does not undergo ESPT. This sharp contrast to GEM-GECO1 confirms the importance of Pro377 for dominant blue emission with Ca^{2+} as the chromophore is effectively trapped in A*. With Arg377, such a trapping effect diminishes and the P377R mutant becomes excitation ratiometric. The resultant biosensor can achieve high imaging contrast by taking the ratio of excitation ratios (e.g., emission at 512 nm with excitations at 450 or 395 nm) of the Ca^{2+}-bound over the Ca^{2+}-free biosensor.[7]

Though the biosensors are thermally equilibrated prior to our spectroscopic measurement, the time-resolved FSRS setup allows the collection of the non-equilibrium chromophore conformational dynamics within the protein pocket following 400 nm photoexcitation. The 800 nm Raman pump is far away from the absorption peaks of both A and B states, so the S_0 Raman peaks are weak (see Fig. 2). However, the A* peaks are pre-resonantly enhanced due to the excited state absorption band around ~900 nm in FPs, previously observed by transient absorption.[10,17,20] This makes it possible to record the excited state spectra without interference from the significant ground state bleaching, and track the evolution of excited state Raman modes during the A*→I* conversion as ESPT occurs.

The time-stacked spectral plot in Fig. 2 contains essential information about transient structural motions during ESPT, and the ~1180, 1545, and 1575 cm^{-1} vibrational bands are analysed to infer the photochemical reaction coordinate that governs biosensor function. The broad baselines for raw data (Fig. S1, ESI†) validate the enhanced S_1 Raman features, while weaker peaks upon Ca^{2+} binding may be due to lower sample concentration, laser pumping efficiency, and varied resonance Raman conditions of the altered chromophore environment. We therefore focus on the kinetic analysis of Fig. 2a and 2b individually. Moreover, in contrast to some other background subtraction methods assuming a one-to-one correspondence to transient absorption features or using complex filters that lead to sharp turns in spectral baselines,[24] our spline fitting method has been field proven to yield reliable results for wild-type GFP and the GEM-GECO1 biosensor,[10,17] which can be compared and cross-checked with the current results.

View Article Online
DOI: 10.1039/C6CP08821J

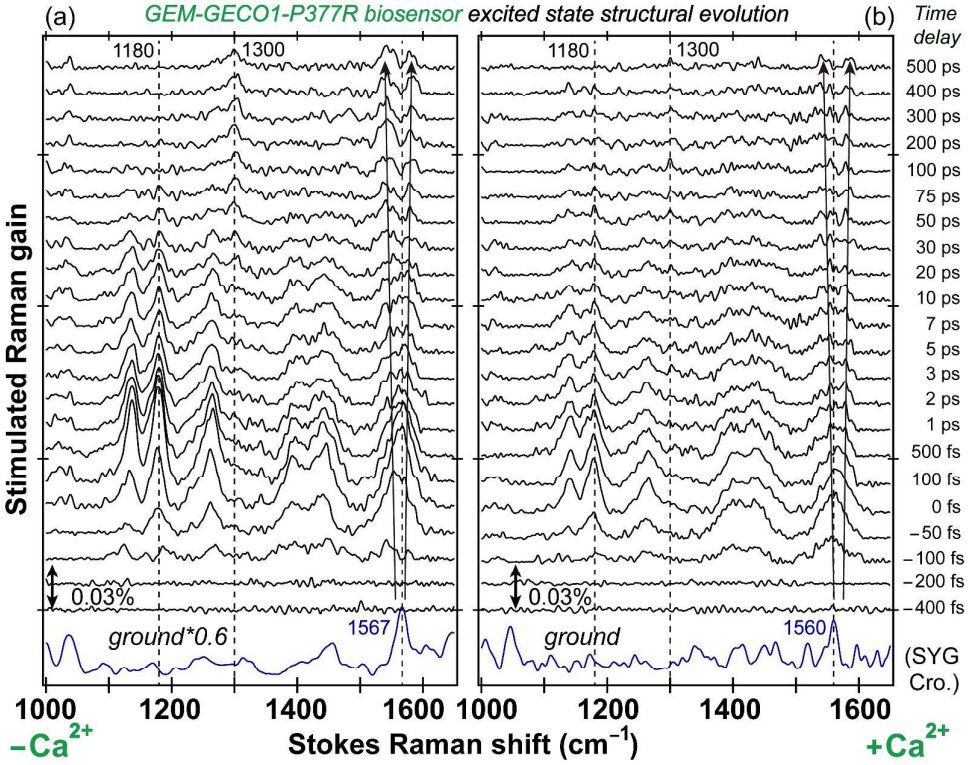

Fig. 2 Time-resolved excited state FSRS of GEM-GECO1-P377R biosensor in the (a) Ca^{2+}-free and (b) Ca^{2+}-bound state from –400 fs to 500 ps after 400 nm photoexcitation. The Raman pump is at 800 nm. The bottom blue trace is the S_0 spectrum with buffer subtracted. The black traces are the excited state spectra with both the ground state and buffer subtracted. The Ca^{2+}-free ground state is scaled by 0.6. The double-headed arrow shows the Raman gain of 0.03%. Peak frequency shifts below 1600 cm^{-1} are denoted by black arrows. Marker bands are labelled by dashed lines.

B. Frequency and intensity dynamics of vibrational marker bands reveal structural inhomogeneity affecting the ESPT pathways

In the electronic ground state S_0, the 1567 cm^{-1} peak is attributed to the phenolic C=C and imidazolinone C=N stretching motions of the chromophore. After 400 nm photoexcitation, this mode shifts and significantly broadens, which can be fit with two peaks and they gradually split with time in S_1. The lower-frequency mode redshifts while the higher-frequency mode blueshifts (Fig. 3). From comparative Gaussian TD-DFT calculations[17,19,25] of the protonated and deprotonated chromophore to assign the observed frequency position and trend, besides the common C=C stretch, the 1545 cm^{-1} mode involves the imidazolinone ring C=N stretch while the 1575 cm^{-1} mode involves the C=O stretch (Table S1, ESI†).

This latter mode is newly observed in this work but not in GEM-GECO1,[17] indicating that the excited state C=O stretching mode is enhanced and further redshifted from its S_0 peak location (~1660 cm^{-1}) due to the P377R mutation. The photoinduced electron redistribution could weaken the double bond and cause the mode frequency redshift. The modified local environment in S_1 may provide additional H-bonding to the C=O bond and also increase its electronic polarizability. After photoexcitation of the Ca^{2+}-free biosensor, this S_1 mode blueshifts from ~1572 to 1584 cm^{-1} with a 37 ps time constant (Fig. 3b). In comparison, the Ca^{2+}-bound biosensor shows a similar blueshift from ~1571 to 1582 cm^{-1} with a 44 ps time constant. Both the trend and rate of the vibrational peak frequency change are consistent with an ESPT reaction that leads to deprotonation of the chromophore. The resultant migration of the negative charge back to the conjugated ring system (see the chromophore chemical structure in the Fig. 1b insert) could increase the C=O double bond character hence the apparent mode frequency blueshift. The ~1 ps dwell time for the exponential fit of the frequency dynamics is similar to other FP biosensors,[17,19-21] confirming that the blueshift is preceded by an initial structural "preparation" stage.[10,26] We consider that during the first 1 ps, the molecular system needs to move out of the FC region with significant electron redistribution and small-scale nuclear motions, which lead to many competing factors and could complicate robust interpretation of the overall unchanged frequency dynamics that are experimentally observed. As I* accumulates, the mode frequency blueshift could involve vibrational cooling in I* state, typically on ps timescale.[27-30] Notably, the 1575 cm^{-1} mode intensity exemplifies complex dynamics (Fig. S2, ESI†) which suggest contributions from both A* and I* states with overlapping vibrational peaks. The double-exponential decay time constants of ~600 fs (16% weight) and 32 ps (84%) are accompanied by a 35 ps rise in the Ca^{2+}-free P377R biosensor.

View Article Online
DOI: 10.1039/C6CP08821J

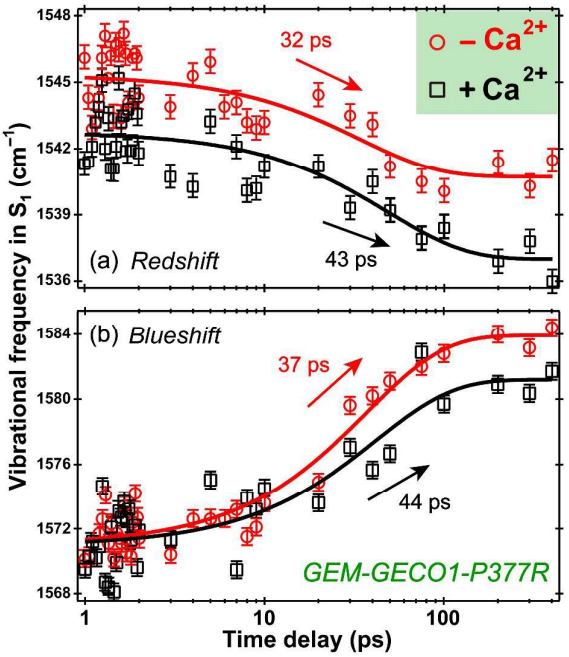

Fig. 3 Time-dependent S_1 vibrational frequency shift tracks transient conformational dynamics. (a) The redshift of the ~1545 cm^{-1} mode in the Ca^{2+}-free and bound P377R biosensor with the 32 and 43 ps time constant, respectively. (b) The blueshift of the ~1575 cm^{-1} mode in the Ca^{2+}-free and bound biosensor with the 37 and 44 ps time constant. The error bars (1 s.d.) are shown. The solid curves are exponential fits.

The lower-frequency mode of this peak doublet redshifts from 1545 to 1541 cm^{-1} and 1543 to 1537 cm^{-1} in the Ca^{2+}-free and bound biosensors, respectively (Fig. 3a). The redshift time constants from the least-squares exponential fit are 32 and 43 ps, which closely match the aforementioned blueshift time constants thus support a common structural dynamics origin.

For further corroboration, we analyse the 1180 cm^{-1} mode intensity dynamics which is also one of the most prominent spectral features in such FP biosensors (see raw data in Fig. S1, ESI†).[17,20] Notably, the Ca^{2+}-free biosensor exhibits a double-exponential decay with 800 fs (60%) and 36 ps (40%) time constants (Fig. 4a) whereas the Ca^{2+}-bound biosensor exhibits a triple-exponential decay with time constants of 660 fs (59%), 16 ps (19%), and 90 ps (22%) (for a less satisfactory double-exponential fit, see Fig. S3, ESI†). The sub-ps time constants are attributed to FC dynamics.[10,17] The 36 ps time constant in the Ca^{2+}-free sample is due to ESPT reaction,[17] similar to the redshift and blueshift time constants in Fig. 3. In comparison, the two ps time constants of the Ca^{2+}-bound biosensor likely arise from two different ESPT pathways. The faster component is attributed to the slightly more deprotonated chromophore population in A* (see the steady-state absorption spectrum in Fig. 1b) and its stabilization by the positively charged Arg377. Our previous work[20,21] on an intensiometric FP biosensor G-GECO1.1 lends support in that a more deprotonated chromophore in the Ca^{2+}-bound state exhibits faster ESPT time constants. The longer, 90 ps time constant is due to the A* subpopulation that is more protonated in S_0, reflected by the blueshifted electronic absorption peak at 392 nm. The apparent time constant of ~44 ps in Fig. 3 is largely consistent with a weighted average of these two distinct ps time constants. We note that these subpopulations arise from the multiple A species underneath a common electronic absorption band with a broad and asymmetric lineshape.

The structural inhomogeneity in the Ca^{2+}-bound biosensor is also inferred in peak widths (Fig. 2). The Ca^{2+}-free peaks are narrower than the Ca^{2+}-bound peaks in general. Because FSRS measures the ensemble average, the observed broader peaks indicate multiple subpopulations. For further comparison, we implement the wavelength-tunable FSRS by keeping the photoexcitation at 400 nm but tuning the Raman pump to 553 nm.[20,31] Due to the pre-resonance match to the stimulated emission band, the I* modes are enhanced (Fig. 4b). Similar to the conventional FSRS data, the Ca^{2+}-free peaks are narrower and close in frequency (1336 and 1370 cm^{-1}) whereas the Ca^{2+}-bound peaks are broader and more separated (1331 and 1383 cm^{-1}) (see the peak width comparison from the least-squares

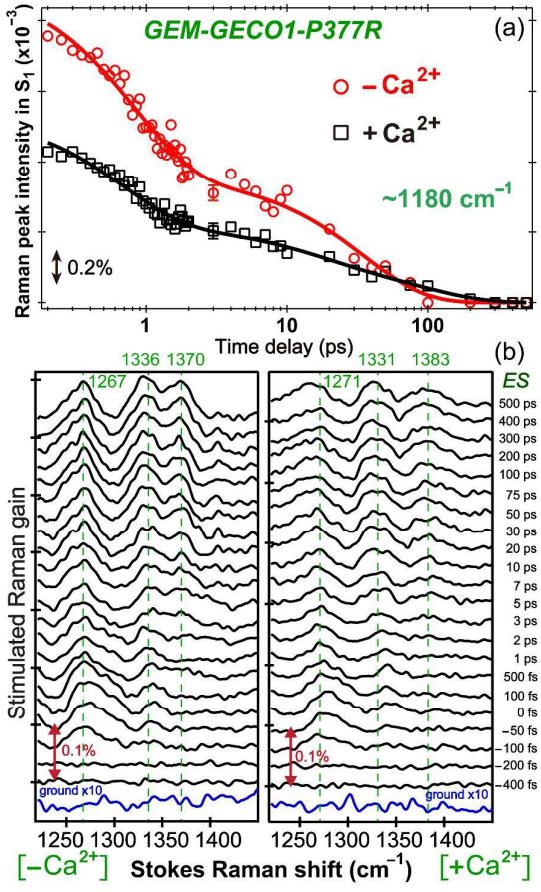

Fig. 4 Intensity dynamics of A* in contrast to I* modes enhanced by tunable FSRS methodology. (a) Integrated intensity plot of the ~1180 cm^{-1} marker bands in Ca^{2+}-free (red circles) and bound (black squares) P377R biosensor from 200 fs to 500 ps. (b) Time-resolved excited state FSRS data of the Ca^{2+}-free and bound biosensor from 1220—1450 cm^{-1} with the Raman pump tuned to 553 nm. The buffer and baseline-subtracted S_0 spectra (blue) are plotted at the bottom and multiplied by 10 to compare with the enhanced transient S_1 spectra (black).

View Article Online
DOI: 10.1039/C6CP08821J

fits in Fig. S4, and major Raman mode assignment in Table S2, ESI†). This result indicates that the two ESPT pathways are largely independent of each other and the resultant transient I* modes do not mix on the ps timescale. Molecular dynamics simulations of GEX-GECO1, a similar excitation-ratiometric Ca^{2+} biosensor with an SYG chromophore and Arg377,[7] support the inhomogeneity seen in P377R biosensor due to two different O···O distances between the chromophore phenolic hydroxyl group and the adjacent Ser118 along the ESPT chain.[17,21] Further analysis of enhanced I* modes will yield insights into the ESPT reaction barrier crossing, vibrational cooling within the I* state, and energy relaxation back to the ground state.

It is clear from the stationary absorption spectrum (Fig. 1) that the P377R biosensor exhibits different ground state chromophore populations including the protonated A (major) and deprotonated B (minor) states. However, that is not the structural inhomogeneity which can be ascertained from the time-resolved FSRS (Figs. 2–4). In fact, because of the choice of actinic pump wavelength at 400 nm, our FSRS spectra only probe the excited state of the protonated species (A* state). In consequence, the above-mentioned A subpopulations govern the ESPT reaction pathways starting from photoexcitation time zero and are thus highly relevant for the biosensor function.

C. Vibrational intensity oscillations on ultrafast timescales dissect the ESPT reaction coordinates

One of the unique resolving powers of excited state FSRS is the direct observation of vibrational quantum beats.[10,13,32-34] Because the Ca^{2+}-free GEM-GECO1 exhibits a dominant 174 cm^{-1} phenolic ring rocking mode that gates ESPT by modulating the distance between proton donor (chromophore hydroxyl) and acceptor (e.g., bridging water molecules), we expect the Ca^{2+}-free P377R biosensor to maintain this pronounced oscillation because the mutation site is far away from the chromophore pocket (Fig. 1a). Indeed, the 1265 cm^{-1} C–O stretch and 1575 cm^{-1} C=C/C=O stretch mode intensities exhibit out-of-phase oscillations that yield a ~184 cm^{-1} mode after fast Fourier transform (FFT) analysis (Fig. 5e). The frequency difference from the 174 cm^{-1} mode in GEM-GECO1 may be due to some long-range interactions in the protein mutant. In contrast, the Ca^{2+}-bound P377R biosensor exhibits weaker and less clear oscillatory patterns with low-frequency modulation modes retrieved at 57, 178, and 267 cm^{-1} (Fig. 5f). The 57 and 267 cm^{-1} modes have phenol ring wagging characters as corroborated by DFT calculations (see below). These modes differ from those in the Ca^{2+}-bound GEM-GECO1 wherein the Pro377 residue inhibits ESPT and leads to

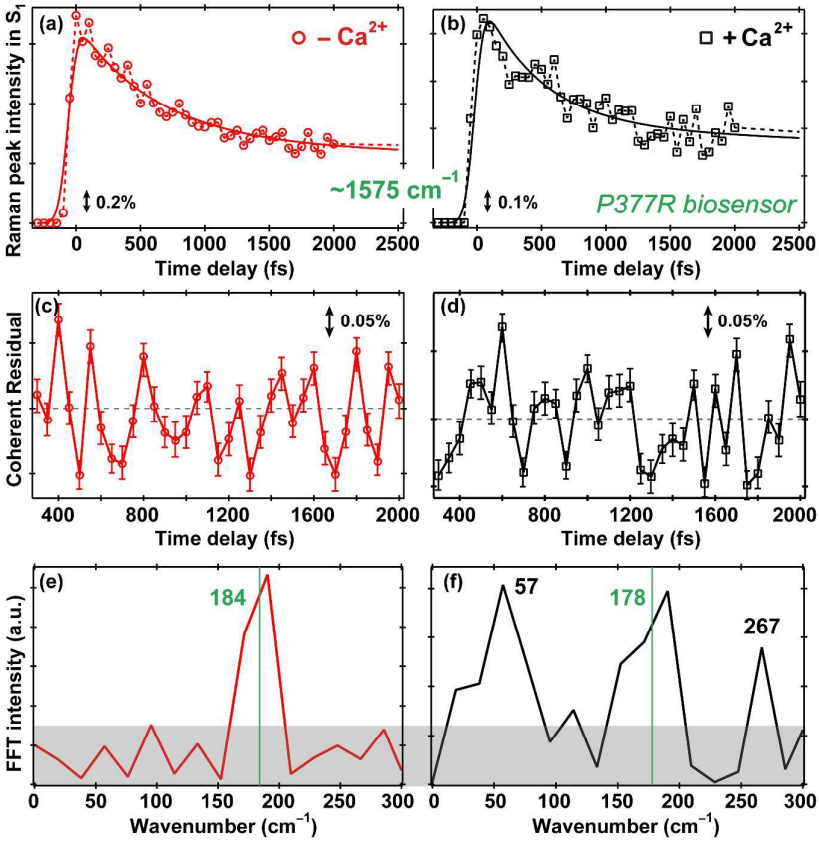

Fig. 5 Transient Raman intensity quantum beats probe low-frequency modulation modes. Integrated intensity dynamics of the ~1575 cm^{-1} mode in (a) Ca^{2+}-free and (b) Ca^{2+}-bound P377R biosensor with data in red circles and black squares, respectively. The corresponding Raman gain magnitude of 0.2% and 0.1% is denoted by the double-arrowed line. After removal of the incoherent rise and decay, e.g., red and black solid fit curves in (a) and (b), the coherent residuals within ~2 ps for (c) Ca^{2+}-free and (d) Ca^{2+}-bound biosensor are displayed. Clearer oscillations occur in (c). Error bars are shown (1 s.d.). The FFT results of the residuals yield dominant modulation modes below ~300 cm^{-1} in the (e) Ca^{2+}-free and (f) Ca^{2+}-bound P377R biosensor, with a conserved low-frequency mode at ~180 cm^{-1}. The FFT experimental noise level is indicated by grey shades.

View Article Online
DOI: 10.1039/C6CP08821J

significant blue fluorescence,[17] which indicates that P377R not only allows the biosensor green fluorescence, it also provides (1) an increased structural inhomogeneity due to less solvent access and less averaging in the chromophore vicinity,[35] (2) multiple ESPT pathways for the chromophore to lose its proton as evidenced by the spectral data analysis of Figs. 2-5, and (3) a more hydrophilic environment with stronger H-bonds involving the positively charged Arg377 residue to help stabilize the deprotonated FP chromophore after ESPT.[20,36]

Notably, the FFT analysis of the Ca^{2+}-free P377R biosensor reveals only one dominant ~184 cm^{-1} mode, which closely matches the chromophore phenol ring rocking mode at ~174 cm^{-1} mode that we observed in the Ca^{2+}-free GEM-GECO1 biosensor (i.e., with the Pro377 residue distant from the GFP chromophore pocket, see structural constraints in Fig. 1a).[17] Since the P377R mutation is far away from the chromophore, it exerts little effect on the local environment around the SYG chromophore, leading to the survival of this functional low-frequency mode with a similar ESPT time constant (~30 ps in the Ca^{2+}-free GEM-GECO1 and 36 ps in the Ca^{2+}-free P377R). In contrast, the FFT analysis of the Ca^{2+}-bound P377R yields a more complex pattern with three low-frequency modes below 300 cm^{-1}. Besides the 178 cm^{-1} mode that is largely conserved and confirms the importance of this in-plane phenol ring rocking motion, the 57 and 267 cm^{-1} modes both have phenol ring out-of-plane wagging character based on DFT calculations in Gaussian.[25] This result indicates that as the Ca^{2+}-bound CaM subunit moves closer, shields the nearby GFP β-barrel opening and increases the inhomogeneity of chromophore pocket (Fig. 1a), additional ESPT pathways are opened because a variety of low-frequency modes are activated and further involved in the vibrational anharmonic coupling matrix.[9,37-39] Because the chromophore conformational states govern the potential energy surface from the electronic ground to excited state, different low-frequency modes are coupled to photoexcitation (starting from the FC region) to various degrees. Their activity in relation to the other anharmonically coupled vibrational motions (e.g., the 1575 cm^{-1} mode in Fig. 5) could act as a molecular gate[10,17,34] and contribute to the observed multiple ESPT rates in the Ca^{2+}-bound biosensor.

In other words, the interplay between the chromophore photoacidity[16,40,41] and the protein local environment particularly the H-bonding network[42-44] determines the dominant photoexcitation energy dissipation pathways along the characteristic vibrational coordinates, out of the FC region, and toward the fluorescent state in these FP-based biosensors.

D. Comparative analysis to previous FP biosensors and within the same biosensor yields key mechanistic underpinnings

A general rule of thumb is that fundamental knowledge could be effectively gained if only one parameter is changed that leads to an observed functionality change. The direct comparison of current work to our previous report[17] on GEM-GECO1 with an identical SYG chromophore provides such a rare opportunity to elucidate the fluorescence modulation mechanism affected by just one strategic interfacial residue between CaM (Ca^{2+}-sensing domain) and GFP (fluorescence domain). We recognize that a multitude of effects could be introduced by one amino acid mutation, from the short-range to long-range interactions, however, we emphasize that this specific mutation close to the protein active site is key to establish the biosensor structure-function relationship because the interfacial residue at position 377 is in close proximity to the embedded chromophore. Our results reveal why GEM-GECO1 is dual-emission ratiometric whereas the P377R mutant is effectively tuned to become single-emission excitation ratiometric, which substantiate the originality and significance of this spectroscopic work.

In a previous report on a green intensiometric G-GECO1.1 biosensor[20] we correlated the consumption of reactant and generation of product state on the tens of ps timescales to a common photochemical reaction coordinate. Similarly, the concomitant observation of A* peak decay and I* peak rise (Fig. 4) in the P377R biosensor well supports the assignment of vibrational dynamics to an ESPT process. Meanwhile, the least-squares fit of the peak frequency shift is considered a reliable way to track the ultrafast photochemical reaction progress particularly when the potentially overlapping Raman modes are along the ESPT reaction coordinate. Alternatively, we can model the observed broad Raman bands near 1545 or 1575 cm^{-1} with two adjacent peaks assigned to A* and I* and fit the apparent frequency shift as a gradual exchange of two distinctive spectral patterns. However, the experimental signal-to-noise ratio and inevitable assumption of the individual peak width could hinder quantitative analysis while the accuracy for such modelling may not surpass the direct fit of peak centre frequency shift.[10,13,45] Therefore, the ensemble nature of FSRS experiments requires a consistent, multifaceted approach to dissect spectral data and deduce reaction mechanisms: the multiple mode frequency dynamics in Fig. 3 need to be compared and discussed in concert with the intensity dynamics of other modes in Fig. 4 so we can firmly attribute the retrieved time constants to the ESPT reaction along with distinguishable conformational states.

Based on these recent findings, we expect that an increase of the hydrophilicity of the protein chromophore pocket with an extended and more flexible H-bonding network could reduce the specific A* subpopulation with the ~90 ps ESPT time constant. The other A* subpopulation that yields the 460 nm emission shoulder band in Fig. 1b (i.e., incapable of undergoing ESPT reaction) could also be decreased. In consequence, the overall fluorescence quantum yield of the Ca^{2+}-bound P377R biosensor can be effectively improved upon 400 nm photoexcitation with the resultant improved biosensor brightness and sensitivity defined as the ratio of excitation ratios for Ca^{2+} sensing.[7]

Experimental

A. Protein sample preparation

The GEM-GECO1-P377R biosensor sample preparation follows previously published procedures starting from *E. coli*

View Article Online
DOI: 10.1039/C6CP08821J

DH10B cells (Invitrogen) transformed with the pTorPE plasmid harbouring the 6-histidine tagged GEM-GECO1.[17] For the single site-specific mutagenesis in this work, the synthetic DNA oligonucleotides with the corresponding sequence were purchased from Integrated DNA Technologies and used with the QuickChange Lightning Single kit (Agilent Technologies). These P377R proteins are harvested, purified, and dissolved in buffer solutions, before finally exchanged into the desired MOPS buffer solution (pH=7.2) with either 10 mM EGTA (for the Ca^{2+}-free sample) or 10 mM Ca-EGTA (for the Ca^{2+}-bound sample). The protein biosensors are characterized by *in vitro* steady-state electronic spectroscopy including the UV-Visible (Thermo Scientific Evolution 201) and fluorescence (Hitachi F-2500) spectrophotometers. To avoid protein destabilization or denaturing, we keep buffer conditions, pH and temperature unchanged and verify the sample integrity using UV-Vis before and after each ultrafast spectroscopic measurement.

We found that three separately prepared batches of purified P377R samples exhibit a weak response to Ca^{2+} in emission under 395 nm excitation. The excitation spectra of P377R suggest this mutant chimeric protein has essentially become an excitation ratiometric (green) indicator, which differs from the original GEM-GECO1 that is a blue-green emission ratiometric biosensor.[17] This result highlights the critical role of residue 377 in the absorption and fluorescence properties of the GCaMP-type indicators for Ca^{2+} sensing.[6,7]

B. Tunable FSRS optical setup

The femtosecond stimulated Raman spectroscopy (FSRS) setup with technical advances in our laboratory has been reported.[15-17,31,46] In brief, a femtosecond (fs) mode-locked Ti:sapphire oscillator (Mantis-5) and regenerative laser amplifier (Legend Elite-USP-1K-HE, Coherent, Inc.) provide ~35 fs, 4 mJ, 800 nm fundamental pulses with a 1 kHz repetition rate. The stimulated Raman pump–probe pair and a preceding actinic pump are separately generated via nonlinear light conversion processes. The 400 nm actinic pulse of ~400 μW arises from the frequency doubling of a portion of the fundamental pulse in a 0.3-mm-thick type-I β-barium borate (BBO) crystal. For conventional FSRS, the 800 nm Raman pump with ~4 mW power and ~3 ps pulse duration is generated by passing the fundamental pulse through a home-built spectral filter.[14,15] The ~100 nJ Raman probe pulse is a supercontinuum white light (ca. 840—960 nm) generated in a 2-mm-thick *Z*-cut sapphire crystal, followed by the prism-pair compression and a long-pass filter (RG830, Newport). For tunable FSRS, the 553 nm Raman pump is produced by a home-built two-stage ps noncollinear optical parametric amplifier (NOPA) which is seeded by an fs NOPA with a spectral filter and pumped by a home-built second harmonic bandwidth compressor.

For the exited state FSRS data collection, the actinic pump is controlled by a motorized translation stage while the Raman pump and probe pulses remain temporally coincident. The three beams are focused on the protein sample solution (OD≈1/mm at 400 nm), continuously flowed through a 1-mm path length quartz cell to avoid thermal effect and provide a fresh spot for pulsed laser irradiation. While the Raman pump and actinic pump pulses are blocked after the sample, the transmitted probe beam carrying the collinear stimulated Raman signal goes through a pinhole and enters an imaging spectrograph (SP-2356, Princeton Instruments). The signal is then dispersed by a 1000 nm blaze, 600 grooves/mm grating in conventional FSRS setup (and a 500 nm blaze, 1200 grooves/mm grating in tunable FSRS) and imaged onto a front-illuminated 1340×100 CCD camera array system (PIXIS 100F; Princeton Instruments). At least 10 sets of excited state FSRS spectra are collected from –5 to 650 ps with various time steps as small as 50 fs. For each time delay point in each spectral data set, 1500 Raman spectra are collected and averaged. Therefore, for the final spectra presented (e.g., Figs. 2 and 4b as well as Fig. S1 in the ESI†), each one data trace represents an average of at least 15000 experimental Raman spectra following photoexcitation. The flowing protein sample spot and incident laser fluctuations within the entire data scan could sporadically exert some small, unwanted effects but the extensive, periodic averaging of the same spectrum at a certain time delay after photoexcitation, being collected at various time during the experiment, could effectively cancel out most of the random noises. The ground state spectrum of the protein biosensor sample is also recorded periodically throughout the excited state data scan to monitor the protein sample and laser stability.[10,15,17,47] The UV-Vis spectra of the samples in buffer solution are collected before and after each FSRS experiment to verify sample integrity (acceptable if the absorption peak intensity variation is within 10% after the entire FSRS experiment on protein samples which typically lasts for 1–2 hours).

Conclusions

In this work, we have developed and implemented the wavelength-tunable excited state FSRS to elucidate the structural dynamics basis for the fluorescence modulation of a single-site P377R mutant of the emergent GEM-GECO1 calcium biosensor. This contribution represents the first time that a targeted single mutant of a functional biosensor is studied by an advanced time-resolved vibrational spectroscopic toolset, especially after the steady-state electronic spectroscopy shows a noticeable difference in its emission properties from the parent biosensor. The transient Raman modes following 400 nm photoexcitation report on the characteristic ESPT time constants of 36 ps in the Ca^{2+}-free biosensor versus 16, 90 ps in the Ca^{2+}-bound state. This covert structural inhomogeneity is a direct consequence of positioning a positively charged residue (like arginine) close to the cpGFP chromophore in response to the Ca^{2+}-binding-induced conformational change at the nearby CaM domain. The altered ESPT pathways based on different H-bonding configurations govern the functionality change from a green-blue emission ratiometric biosensor (GEM-GECO1) to a green excitation ratiometric biosensor (GEM-GECO1-P377R) for Ca^{2+} imaging. Such a quantitative examination of the molecular mechanism provides previously unavailable knowledge about this emerging calcium biosensor

View Article Online
DOI: 10.1039/C6CP08821J

family, particularly regarding the intrinsic conformational states and molecular motions of the functional chromophore.

Furthermore, from the integrated Raman peak intensity oscillations, a chromophore in-plane ring rocking mode at ~180 cm^{-1} is found to dominate in the Ca^{2+}-free biosensor but is joined by two other out-of-plane low-frequency modes in gating the multidimensional ESPT reaction coordinate upon Ca^{2+} binding. We expect that such targeted mutation(s) around the protein active site, in conjunction with the genetic code expansion methods to incorporate various non-canonical amino acids[48,49] as well as chemical modification of the chromophores,[41,50] can efficiently translate the rational design principles uncovered by ultrafast Raman spectroscopy into better FP biosensors for advanced bioimaging applications.

Acknowledgements

This work was supported in part by the U.S. National Science Foundation CAREER grant (CHE-1455353). We thank Breland Oscar and Nikita Rozanov for discussions, and Dr. Yongxin Zhao and Prof. Robert E. Campbell (University of Alberta, Canada) for providing the purified and concentrated GEM-GECO1-P377R protein biosensor samples with the targeted mutation.

Notes and references

1 O. Shimomura, *FEBS Lett.*, 1979, **104**, 220-222.
2 M. Chalfie, Y. Tu, G. Euskirchen, W. W. Ward and D. C. Prasher, *Science*, 1994, **263**, 802-805.
3 R. Y. Tsien, *Annu. Rev. Biochem.*, 1998, **67**, 509-544.
4 H.-w. Ai, K. L. Hazelwood, M. W. Davidson and R. E. Campbell, *Nat. Methods*, 2008, **5**, 401-403.
5 G. Jung, (Ed.), *Fluorescent Proteins II: Application of Fluorescent Protein Technology*, Springer-Verlag, Berlin Heidelberg, 2012.
6 A. Miyawaki, J. Llopis, R. Heim, J. M. McCaffery, J. A. Adams, M. Ikura and R. Y. Tsien, *Nature*, 1997, **388**, 882-887.
7 Y. Zhao, S. Araki, J. Wu, T. Teramoto, Y.-F. Chang, M. Nakano, A. S. Abdelfattah, M. Fujiwara, T. Ishihara, T. Nagai and R. E. Campbell, *Science*, 2011, **333**, 1888-1891.
8 R. J. D. Miller, *Science*, 2014, **343**, 1108-1116.
9 R. M. Hochstrasser, *Proc. Natl. Acad. Sci. U.S.A.*, 2007, **104**, 14190-14196.
10 C. Fang, R. R. Frontiera, R. Tran and R. A. Mathies, *Nature*, 2009, **462**, 200-204.
11 H. Kuramochi, S. Takeuchi and T. Tahara, *J. Phys. Chem. Lett.*, 2012, **3**, 2025-2029.
12 J. T. M. Kennis, I. H. M. van Stokkum, D. S. Peterson, A. Pandit and R. M. Wachter, *J. Phys. Chem. B*, 2013, **117**, 11134-11143.
13 D. P. Hoffman and R. A. Mathies, *Acc. Chem. Res.*, 2016, **49**, 616-625.
14 D. W. McCamant, P. Kukura, S. Yoon and R. A. Mathies, *Rev. Sci. Instrum.*, 2004, **75**, 4971-4980.
15 W. Liu, F. Han, C. Smith and C. Fang, *J. Phys. Chem. B*, 2012, **116**, 10535-10550.
16 W. Liu, Y. Wang, L. Tang, B. G. Oscar, L. Zhu and C. Fang, *Chem. Sci.*, 2016, **7**, 5484-5494.
17 B. G. Oscar, W. Liu, Y. Zhao, L. Tang, Y. Wang, R. E. Campbell and C. Fang, *Proc. Natl. Acad. Sci. U.S.A.*, 2014, **111**, 10191-10196.
18 D. Zhong, A. Douhal and A. H. Zewail, *Proc. Nat. Acad. Sci. U.S.A.*, 2000, **97**, 14056-14061.
19 Y. Wang, L. Tang, W. Liu, Y. Zhao, B. G. Oscar, R. E. Campbell and C. Fang, *J. Phys. Chem. B*, 2015, **119**, 2204-2218.
20 L. Tang, W. Liu, Y. Wang, Y. Zhao, B. G. Oscar, R. E. Campbell and C. Fang, *Chem. Eur. J.*, 2015, **21**, 6481-6490.
21 L. Tang, W. Liu, Y. Wang, L. Zhu, F. Han and C. Fang, *J. Phys. Chem. Lett.*, 2016, **7**, 1225-1230.
22 J. Akerboom, J. D. V. Rivera, M. M. R. Guilbe, E. C. A. Malavé, H. H. Hernandez, L. Tian, S. A. Hires, J. S. Marvin, L. L. Looger and E. R. Schreiter, *J. Biol. Chem.*, 2009, **284**, 6455-6464.
23 J. Akerboom, T.-W. Chen, T. J. Wardill, L. Tian, J. S. Marvin, S. Mutlu, N. C. Calderón, F. Esposti, B. G. Borghuis, X. R. Sun, A. Gordus, M. B. Orger, R. Portugues, F. Engert, J. J. Macklin, A. Filosa, A. Aggarwal, R. A. Kerr, R. Takagi, S. Kracun, E. Shigetomi, B. S. Khakh, H. Baier, L. Lagnado, S. S.-H. Wang, C. I. Bargmann, B. E. Kimmel, V. Jayaraman, K. Svoboda, D. S. Kim, E. R. Schreiter and L. L. Looger, *J. Neurosci.*, 2012, **32**, 13819-13840.
24 M. Quick, A. L. Dobryakov, S. A. Kovalenko and N. P. Ernsting, *J. Phys. Chem. Lett.*, 2015, **6**, 1216-1220.
25 M. J. Frisch, G. W. Trucks, H. B. Schlegel, G. E. Scuseria, M. A. Robb, J. R. Cheeseman, G. Scalmani, V. Barone, B. Mennucci, G. A. Petersson, H. Nakatsuji, M. Caricato, X. Li, H. P. Hratchian, A. F. Izmaylov, J. Bloino, G. Zheng, J. L. Sonnenberg, M. Hada, M. Ehara, K. Toyota, R. Fukuda, J. Hasegawa, M. Ishida, T. Nakajima, Y. Honda, O. Kitao, H. Nakai, T. Vreven, J. J. A. Montgomery, J. E. Peralta, F. Ogliaro, M. Bearpark, J. J. Heyd, E. Brothers, K. N. Kudin, V. N. Staroverov, R. Kobayashi, J. Normand, K. Raghavachari, A. Rendell, J. C. Burant, S. S. Iyengar, J. Tomasi, M. Cossi, N. Rega, J. M. Millam, M. Klene, J. E. Knox, J. B. Cross, V. Bakken, C. Adamo, J. Jaramillo, R. Gomperts, R. E. Stratmann, O. Yazyev, A. J. Austin, R. Cammi, C. Pomelli, J. W. Ochterski, R. L. Martin, K. Morokuma, V. G. Zakrzewski, G. A. Voth, P. Salvador, J. J. Dannenberg, S. Dapprich, A. D. Daniels, Ö. Farkas, J. B. Foresman, J. V. Ortiz, J. Cioslowski and D. J. Fox, *Gaussian 09, Revision B.1*, Gaussian, Inc., Wallingford, CT, 2009.
26 F. Han, W. Liu and C. Fang, *Chem. Phys.*, 2013, **422**, 204-219.
27 T. Lian, B. Locke, Y. Kholodenko and R. M. Hochstrasser, *J. Phys. Chem.*, 1994, **98**, 11648-11656.
28 P. Hamm, S. M. Ohline and W. Zinth, *J. Chem. Phys.*, 1997, **106**, 519-529.
29 Y. Mizutani and T. Kitagawa, *Science*, 1997, **278**, 443-446.
30 S. A. Kovalenko, R. Schanz, H. Hennig and N. P. Ernsting, *J. Chem. Phys.*, 2001, **115**, 3256-3273.
31 L. Zhu, W. Liu and C. Fang, *Appl. Phys. Lett.*, 2014, **105**, 041106.
32 A. H. Zewail, *Femtochemistry: Ultrafast Dynamics of the Chemical Bond*, World Scientific, Singapore, 1994.
33 D. B. Turner, K. E. Wilk, P. M. G. Curmi and G. D. Scholes, *J. Phys. Chem. Lett.*, 2011, **2**, 1904-1911.
34 P. J. M. Johnson, A. Halpin, T. Morizumi, V. I. Prokhorenko, O. P. Ernst and R. J. D. Miller, *Nature Chem.*, 2015, **7**, 980-986.
35 C. Fang, A. Senes, L. Cristian, W. F. DeGrado and R. M. Hochstrasser, *Proc. Natl. Acad. Sci. U.S.A.*, 2006, **103**, 16740-16745.

View Article Online
DOI: 10.1039/C6CP08821J

36 X. Shi, P. Abbyad, X. Shu, K. Kallio, P. Kanchanawong, W. Childs, S. J. Remington and S. G. Boxer, *Biochemistry*, 2007, **46**, 12014-12025.
37 M. H. Vos, F. Rappaport, J.-C. Lambry, J. Breton and J.-L. Martin, *Nature*, 1993, **363**, 320-325.
38 Q. Wang, R. W. Schoenlein, L. A. Peteanu, R. A. Mathies and C. V. Shank, *Science*, 1994, **266**, 422-424.
39 L. Zhu, J. T. Sage and P. M. Champion, *Science*, 1994, **266**, 629-632.
40 R. Simkovitch, S. Shomer, R. Gepshtein and D. Huppert, *J. Phys. Chem. B*, 2015, **119**, 2253-2262.
41 S. P. Laptenok, J. Conyard, P. C. B. Page, Y. Chan, M. You, S. R. Jaffrey and S. R. Meech, *Chem. Sci.*, 2016, **7**, 5747-5752.
42 A. Douhal, F. Lahmani and A. H. Zewail, *Chem. Phys.*, 1996, **207**, 477-498.
43 M. Rini, B.-Z. Magnes, E. Pines and E. T. J. Nibbering, *Science*, 2003, **301**, 349-352.
44 E. R. Young, J. Rosenthal, J. M. Hodgkiss and D. G. Nocera, *J. Am. Chem. Soc.*, 2009, **131**, 7678-7684.
45 Y.-C. Wu, B. Zhao and S.-Y. Lee, *J. Chem. Phys.*, 2016, **144**, 054104.
46 W. Wang, W. Liu, I.-Y. Chang, L. A. Wills, L. N. Zakharov, S. W. Boettcher, P. H.-Y. Cheong, C. Fang and D. A. Keszler, *Proc. Natl. Acad. Sci. U.S.A.*, 2013, **110**, 18397-18401.
47 R. R. Frontiera, C. Fang, J. Dasgupta and R. A. Mathies, *Phys. Chem. Chem. Phys.*, 2012, **14**, 405-414.
48 L. Wang, J. M. Xie, A. A. Deniz and P. G. Schultz, *J. Org. Chem.*, 2003, **68**, 174-176.
49 J. C. Peeler and R. A. Mehl, in *Unnatural Amino Acids*, eds. L. Pollegioni and S. Servi, Humana Press, 2012, ch. 8, pp. 125-134.
50 C. L. Walker, K. A. Lukyanov, I. V. Yampolsky, A. S. Mishin, A. S. Bommarius, A. M. Duraj-Thatte, B. Azizi, L. M. Tolbert and K. M. Solntsev, *Curr. Opin. Chem. Biol.*, 2015, **27**, 64-74.